ADVANCED MATERIALS

Supporting Information

for *Adv. Mater.*, DOI 10.1002/adma.202301321

Highly Reliable Textile-Type Memristor by Designing Aligned Nanochannels

Yue Liu, Xufeng Zhou, Hui Yan, Xiang Shi, Ke Chen, Jinyang Zhou, Jialin Meng, Tianyu Wang, Yulu Ai, Jingxia Wu, Jiaxin Chen, Kaiwen Zeng, Lin Chen, Yahui Peng, Xuemei Sun, Peining Chen* and Huisheng Peng**

Supporting Information for

Highly reliable textile-type memristor by designing aligned nanochannels

Yue Liu, Xufeng Zhou, Hui Yan, Xiang Shi, Ke Chen, Jinyang Zhou, Jialin Meng, Tianyu Wang, Yulu Ai, Jingxia Wu, Jiaxin Chen, Kaiwen Zeng, Lin Chen, Yahui Peng, Xuemei Sun, Peining Chen* and Huisheng Peng**

Y. Liu, Dr. X. Zhou, Dr. X. Shi, K. Chen, J. Zhou, Y. Ai, Dr. J. Wu, Dr. K. Zen, Prof. X. Sun, Prof. P. Chen, Prof. H. Peng
State Key Laboratory of Molecular Engineering of Polymers, Department of Macromolecular Science and Laboratory of Advanced Materials, Fudan University, Shanghai 200438, China, E-mail: peiningc@fudan.edu.cn; penghs@fudan.edu.cn.

Dr. J. Meng, Dr. T. Wang, Prof. L. Chen
State Key Laboratory of ASIC and System, School of Microelectronics, Fudan University, Shanghai 200433, China, E-mail: linchen@fudan.edu.cn.

H. Yan, Prof. Y. Peng
School of Electronic and Information Engineering, Beijing Jiaotong University, Beijing 100044, China

Dr. J. Chen
Department of Materials Science, Fudan University, Shanghai 200433, China

This file includes:

Materials and Methods

1. Preparation of Pt/CuZnS fibers

The CuZnS film was deposited onto Pt fiber electrode through the chemical bath deposition method[1]. To deposit CuZnS film without nanochannels, first, three precursor solutions were prepared as follows: mixed solution (namely Solution A) consisting of $CuSO_4 \cdot 5H_2O$ (0.375 mmol) and $Zn(CH_3COO)_2 \cdot 2H_2O$ (4.625 mmol) dissolved in the deionized water (50 mL), $Na_2EDTA \cdot 2H_2O$ (1.4 mmol) dissolved in the deionized water (25 mL) (namely Solution B) and C_2H_5NS (4.0 mmol) dissolved in the deionized water (25 mL) (namely Solution C). Then, solution B was added to solution A and sonicated for 30 min, in which Pt fiber electrodes (diameter of 50 μm, 99.99%) were placed. The CuZnS film was deposited on Pt fiber electrodes after adding Solution C to the above mixed solution and constantly stirred at 70 °C for 1 h. Finally, the deposited Pt fibers were rinsed in the deionized water and dried at 80 °C. In the deposition process, $EDTA^{2-}$ could coordinate with Cu^{2+} and Zn^{2+} to form Cu^{2+} and Zn^{2+} complexes, which regulated the release rate of Cu^{2+} and Zn^{2+} to adjust the growth process of CuZnS film, thus promoting the formation of nanochannels[2]. Therefore, the CuZnS films with nanochannels having different sizes were achieved by adjusting the amount of $Na_2EDTA \cdot 2H_2O$ (1.0 mmol, 0.8 mmol and 0.5 mmol).

2. Fabrication of textile-type memristors

The Pt/CuZnS fibers (diameter of 50 μm, 99.99%) were interwoven with another Ag fibers (diameter of 20 μm, 99.99%) to construct flexible textile-type memristors, where each interlaced point between Pt/CuZnS and Ag fibers functioned as an individual memristor unit. The weave diagram is presented in Figure 1c and d. Note that other fiber materials such as cotton thread can be also co-woven inside.

3. Fabrication of fiber sensor to detect ultraviolet light

The fiber sensor for ultraviolet light detection was fabricated according to the previous literature[3]. First, TiO_2 nanotubes serving as UV-light responsive layer were deposited onto the Ti fiber (diameter of 127 μm, 99.99%) by anodization method, where ethylene glycol electrolyte solution containing NH_4F (0.3 wt%) and deionized water (8 wt%) was used. The pure Ti fiber was used as the anode to oxidize in the above electrolyte solution at 40 ^oC for 30 min (the Pt plate was used as the cathode). After the anodization process, the modified Ti fiber was rinsed in deionized water and

annealed at 500 °C in air for 1 h. Then the CuZnS film serving as a hole-transport layer was deposited on the modified Ti fiber. Finally, carbon nanotube fiber was carefully twisted with the fabricated composite fiber to form a fiber sensor for ultraviolet light detection (Figure S19, Supporting Information).

4. Fabrication of fiber triboelectric sensor

The fiber triboelectric sensor was fabricated by using a twisting method according to the previous literature[4,5]. For instance, five common stainless-steel fibers (diameter of 20 μm) were chosen to be the core fiber working as the inner electrode. Afterward, by twisting the stainless-steel fibers with several polyester fibers acting as triboelectric layers, the fiber triboelectric sensor was fabricated. Finally, the fiber triboelectric sensor was sewn into the inner surface of commercial fingerstall for wearable uses (Figure S20, Supporting Information).

5. Fabrication of electroluminescent textile display

The electroluminescent display on a coat was fabricated by sewing electroluminescent yarns[6]. First, a layer of electroluminescent slurry (a mixture of ZnS phosphors and waterborne polyurethane with a weight ratio of 3:1) was repeatedly dip-coated on silver-plated nylon yarns. After the drying process, the ZnS-coated yarns were twisted with the enameled copper yarns serving as the counter electrode to form electroluminescent yarns.

6. Electrical measurements and characterizations

The electrical measurements of the memristors including direct current and pulse electrical measurements were performed in ambient air using the semiconductor characterization system (Keithley2400 and 4200). The optoelectronic properties of ultraviolet light fiber sensor were collected with the semiconductor characterization system (Keithley 4200-SCS), and the 70 W xenon arc lamp with a monochromator was used as the light source. The light intensity was measured with the NOVA II power meter (OPHIR photonics). The open-circuit voltage of fiber triboelectric sensor was measured by the Keithley meter (Keithley 2614B). The ultraviolet-light-monitoring-feedback cloth was tested with the simulated ultraviolet light from a solar simulator. The intensity could be varied by different attenuators. The Mott−Schottky measurement was conducted by the CHI 760D electrochemical workstation.

The morphologies were characterized by field-emission scanning electron microscopy (SEM, Zeiss Gemini SEM500), energy-dispersive X-ray spectroscopy (Aztec X-Max Extreme), atomic force microscopy (Fast-scan) and high-resolution transmission electron microscope (TEM, JEOL JEM-2100F). The surface potential was varied by Kelvin probe force microscopy with a Pt/Ir5-coated silicon tip. The chemical composition and structure were confirmed by X-ray diffraction spectroscopy (Bruker AXSD8) and X-ray photoelectron spectroscope (XPS, PHI5300). The Cu K-edge synchrotron radiation X-ray absorption fine structure spectroscopy (XAFS) measurements were performed on the 1W1B beamline of the Beijing Synchrotron Radiation Facility (BSRF), China. The S-defect or vacancy was varied by electron paramagnetic resonance (Bruker A300) and aberration-corrected scanning transmission electron microscopy (JEM-ARM300F). The orientation of the nanochannels was characterized by grazing-incidence small-angle X-ray scattering (Xeuss2.0). Photographs were taken by a camera (SONY A6000, Japan).

The neural network simulation[7,8] was conducted on the basis of the platform CrossSim. A three-layer (one hidden layer) neural network was used to perform supervised learning over the learning examples with back-propagation, after which the network recognition accuracy was estimated by inferring separate testing examples.

7. Computational method and model

The calculations were carried out with Cambridge Sequential Total Energy Package (CASTEP) code in the framework of density functional theory [9]. Specifically, the Perdew-Burke-Ernzerhof exchange-correlation functional[10] within the generalized gradient approximation was employed to describe the exchange-correlation energy. Geometric convergence tolerances were set for maximum force of 0.03 eV/A˚, maximum energy change of 10^{-5} eV/atom, maximum displacement of 0.001 A˚ and maximum stress of 0.5 GPa. The sampling in the Brillouin zone was set with 3×3×1 for S defect generation energy, 4×4×3 for bulk diffusion of Ag ions and 3×3×1 for surface diffusion of Ag ions by the Monkhorst-Pack method.

The diffusion of Ag ion was investigated by searching the possible diffusion route and identifying the migration transition state with the lowest diffusion energy barrier. The

diffusion energy barrier is the energy difference between the total energies of transition state and the initial structure. The transition state is searched by the generalized synchronous transit (LST/QST) method[11] implemented in the CASTEP code. The algorithm started from a linear synchronous transit (LST) optimization, and continued with a quadratic synchronous transit (QST) maximization process. Thereafter, the conjugate gradient (CG) minimization was conducted from the obtained LST/QST structure to refine the geometry of transition state. The LST/QST/CG calculations were repeated till a stable transition state is obtained.

8. Statistical analysis

The set voltage variation is defined as the standard deviation of set voltage divided by its average value. The size of nanochannels in the film was presented as the mean ± standard deviation of total nanochannel sizes in SEM image. The size of grain on the fiber electrode was presented as the mean ± standard deviation of total grain sizes in metallographic image.

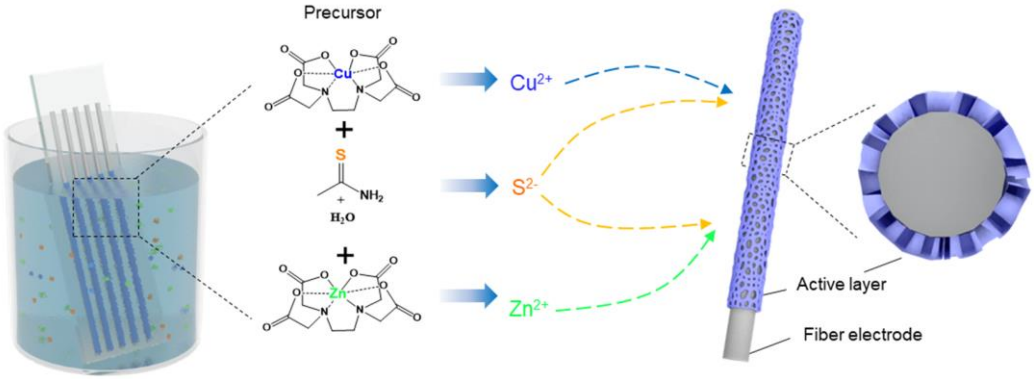

Figure S1. Schematic showing chemical bath method to deposit CuZnS film on Pt fiber. $EDTA^{2-}$ could coordinate with Cu^{2+} and Zn^{2+} to form complexes, and regulate the deposition process of CuZnS film to form nanochannels.

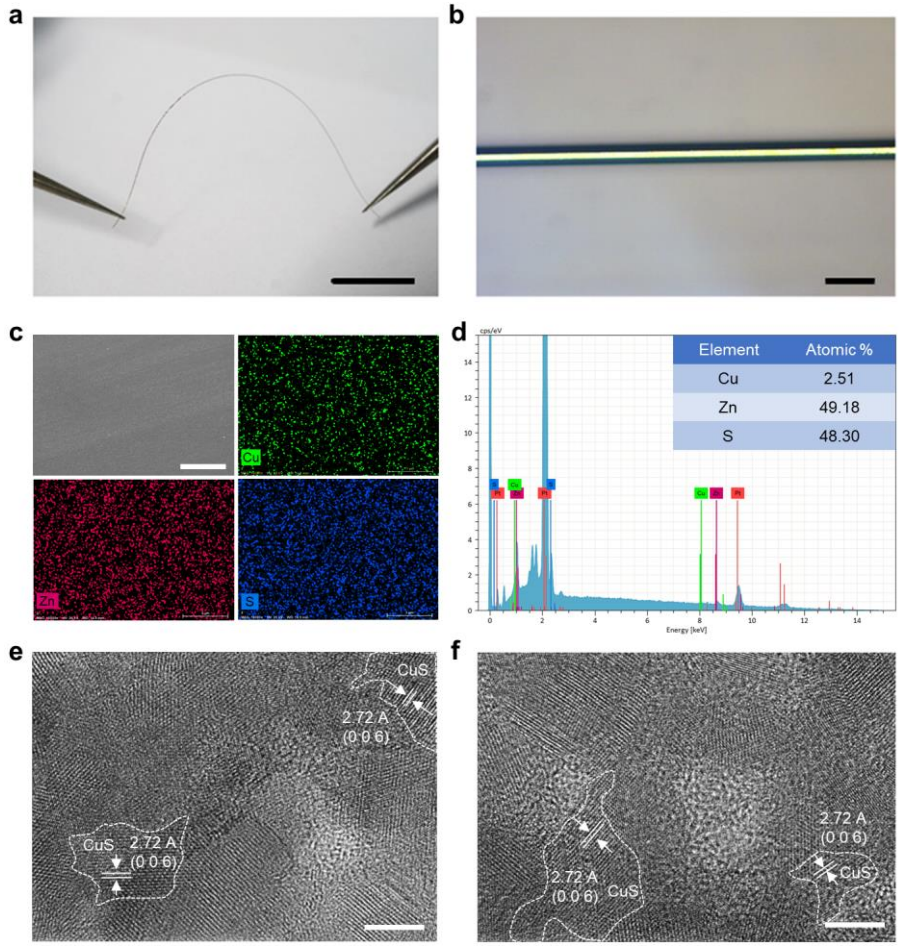

Figure S2. a) Photograph of bent Pt fiber electrode deposited with CuZnS film. b) Optical microscope image of Pt/CuZnS fiber. c) SEM and energy-dispersive X-ray spectroscopy images of Pt/CuZnS fiber. d) Atomic ratio of Pt/CuZnS fiber. e, f) TEM images of CuZnS film at different positions. The CuS phases were screened and marked with dashed line. Scale bars, 1.0 cm (a), 100 μm (b), 3 μm (c), 5 nm (e), 5 nm (f).

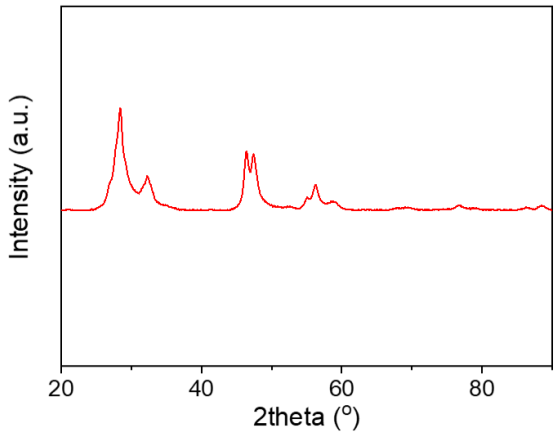

Figure S3. X-ray diffraction pattern of CuZnS film.

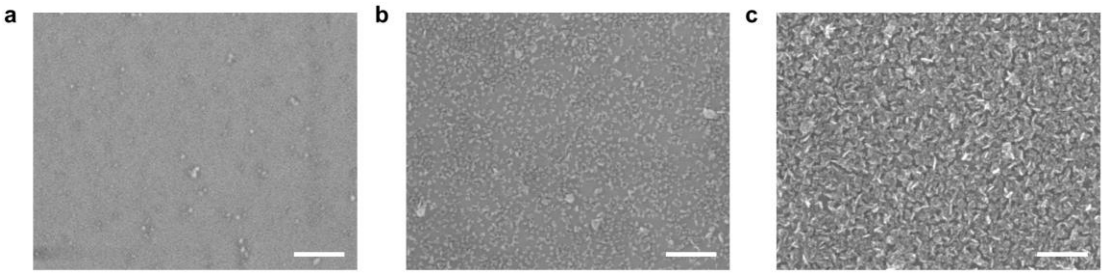

Figure S4. SEM images for the depositing process of CuZnS film for (a) 5 min, (b) 10 min, (c) 30 min. Scale bars, 200 nm.

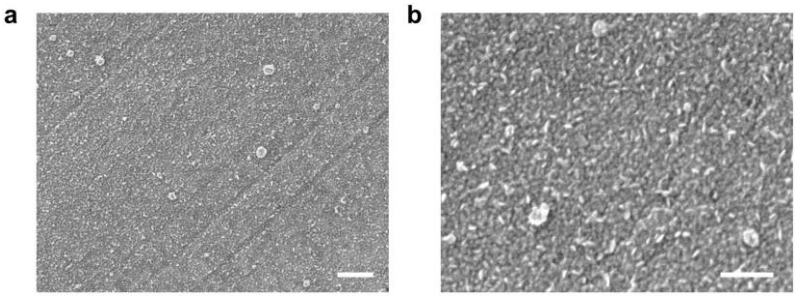

Figure S5. a, b) SEM images of CuZnS film without nanochannels. Scale bars, 400 nm (a), 200 nm (b).

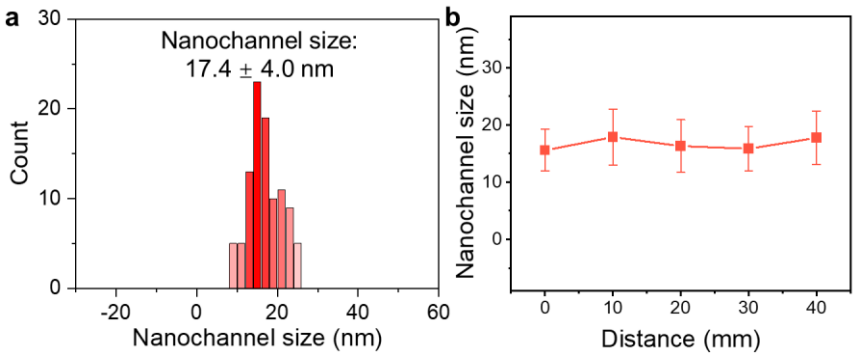

Figure S6. a) Statistical distribution of nanochannel size. The average size was 17.4 nm. b) Statistical average size of nanochannels in the memristive layer at different positions along the fiber electrode. The error bar represents the standard deviation.

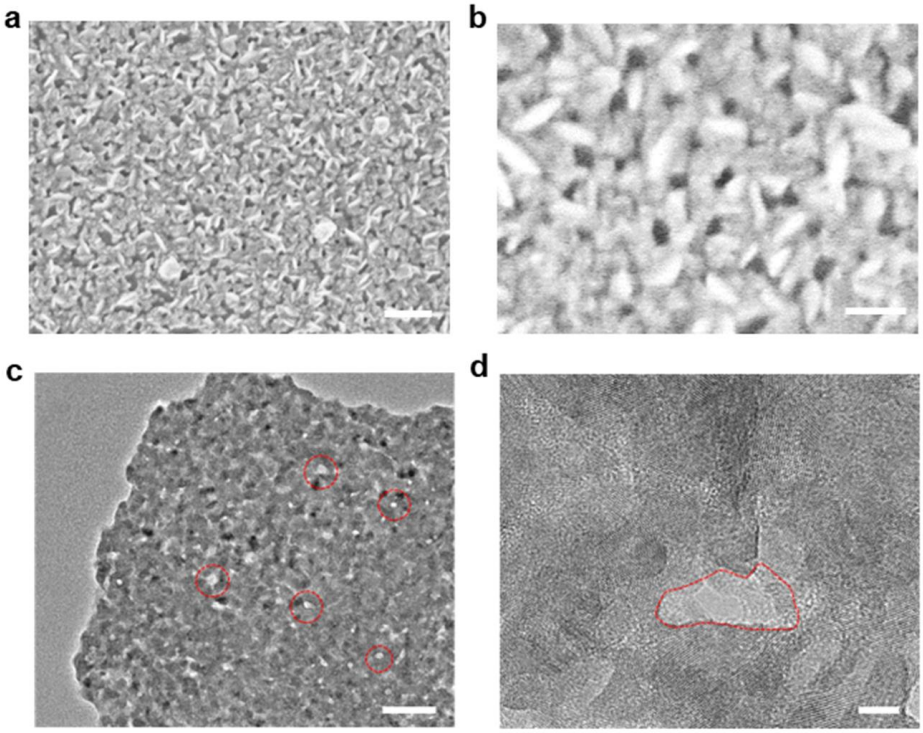

Figure S7. a, b) SEM images of CuZnS film with nanochannels (average size of ~17.4 nm). c, d) TEM images of CuZnS film with nanochannels at low and high magnifications, respectively. Representative nanochannels are marked with red dotted circles. Scale bars, 200 nm (a), 50 nm (b, c), 5 nm (d).

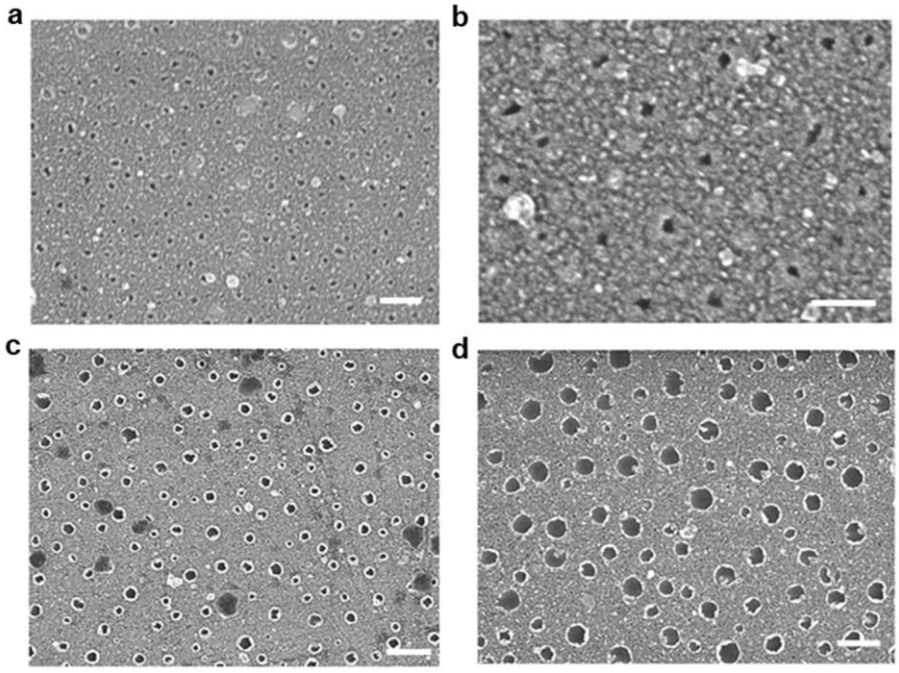

Figure S8. SEM images of CuZnS film with nanochannels having average size of approximately 50 nm (a, b) and 200 nm (c, d). Scale bars, 400 nm (a, d), 200 nm (b), 1 μm (c).

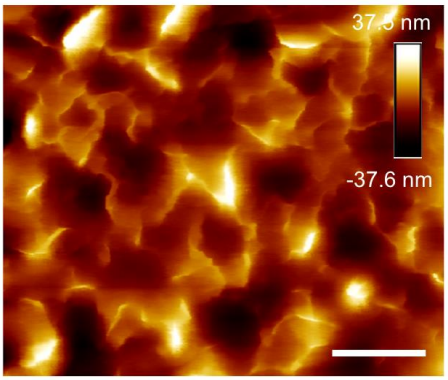

Figure S9. Atomic force microscopy image (AFM) of the CuZnS film with nanochannels. Scale bar, 50 nm.

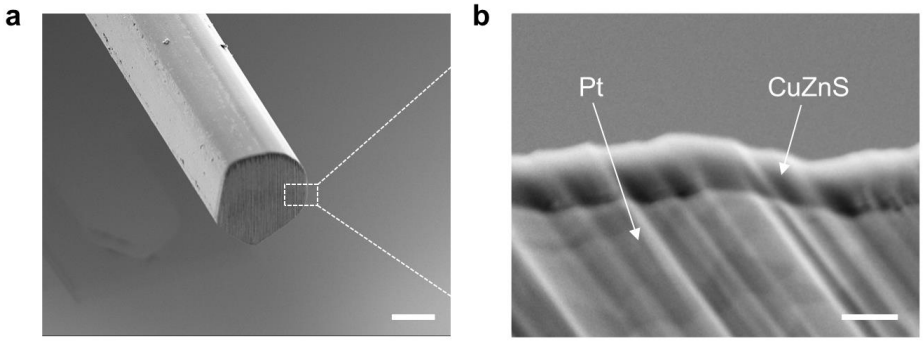

Figure S10. Cross-sectional SEM image of Pt/CuZnS fiber (a) and its enlarged view (b). Scale bar, 20 μm (a), 50 nm (b).

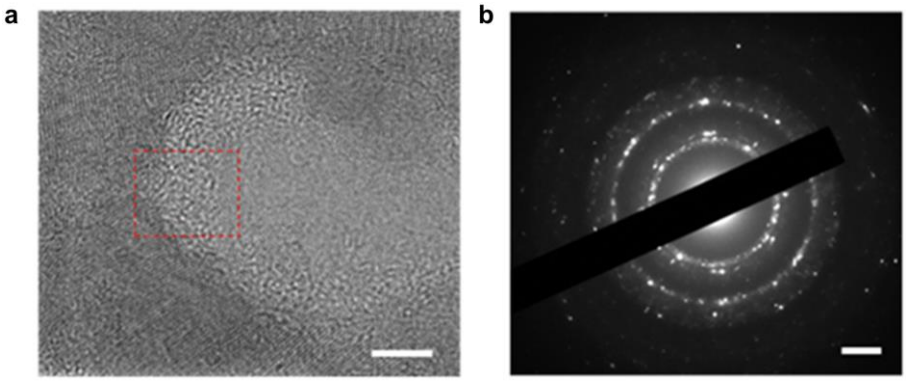

Figure S11. a) TEM image of nanochannel in the CuZnS film. b) Selected area electron diffraction pattern of CuZnS film with nanochannels. Scale bars, 5 nm (a), 2 1/nm (b).

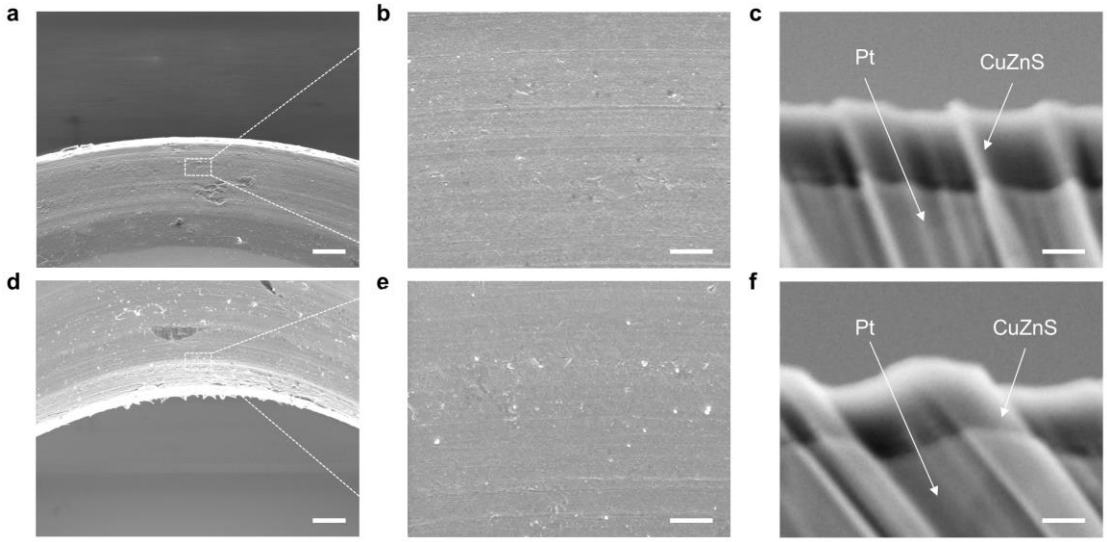

Figure S12. a-c) SEM images of Pt/CuZnS fiber at the top with increasing magnifications as it was bent with a curvature radius of 0.1 mm. d-f) SEM images of Pt/CuZnS fiber at the bottom with increasing magnifications as it was bent with a curvature radius of 0.1 mm. Figures c and f are the cross-sectional view. Scale bars, 10 μm (a, d), 1.0 μm (b, e), 25 nm (c, f).

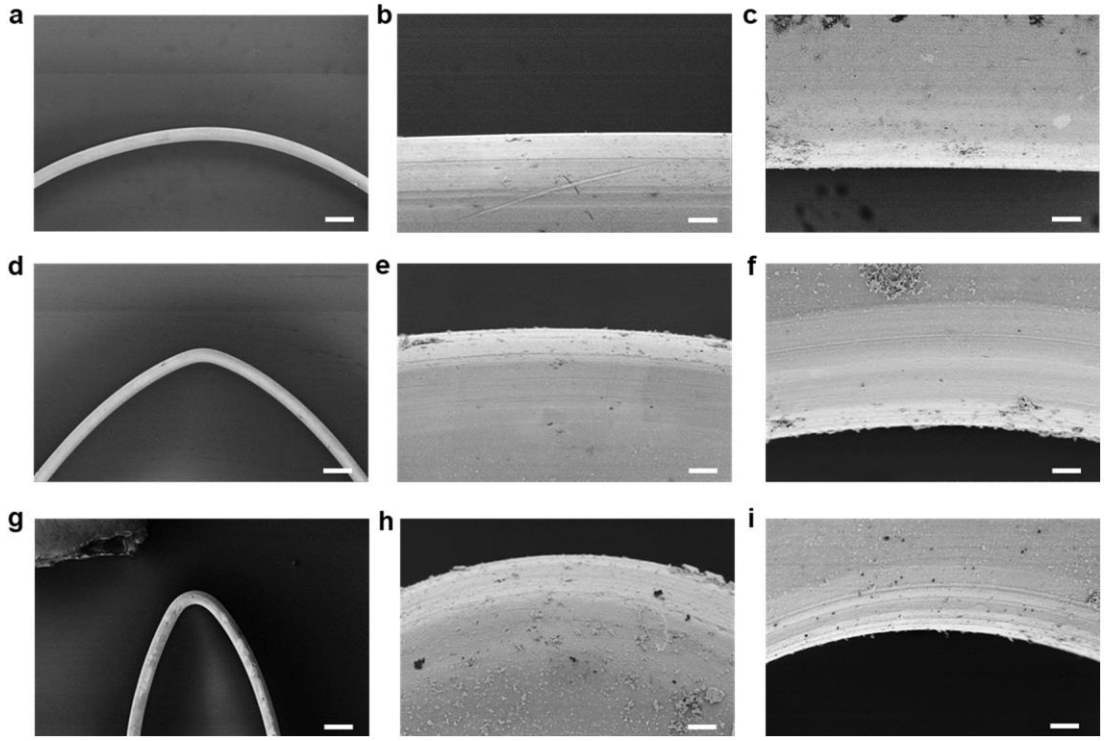

Figure S13. a-c) SEM images of Pt/CuZnS fiber bent with a curvature radius of 1.5 mm. d-f) SEM images of Pt/CuZnS fiber bent with a curvature radius of 0.8 mm. g-i) SEM images of Pt/CuZnS fiber bent with a curvature radius of 0.3 mm. Scale bars, 100 μm (a, d, g), 4.0 μm (b, c, e, f, h, i).

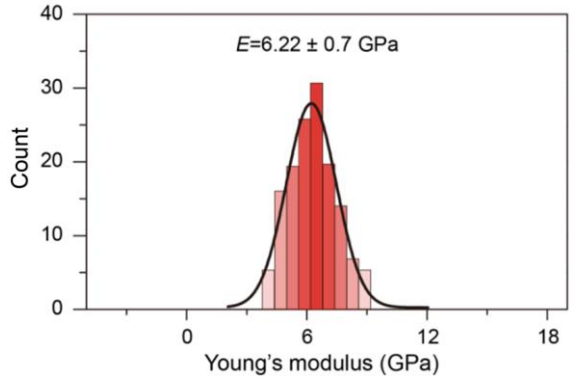

Figure S14. The distribution of Young's modulus for CuZnS films with nanochannels.

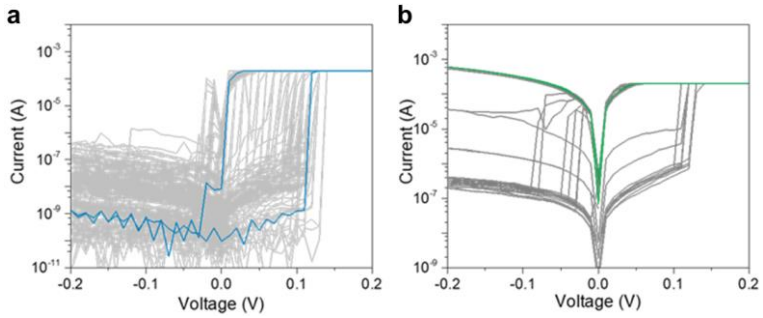

Figure S15. *I-V* curves of textile-type memristor units with nanochannel size of 50 (a) and 200 nm (b).

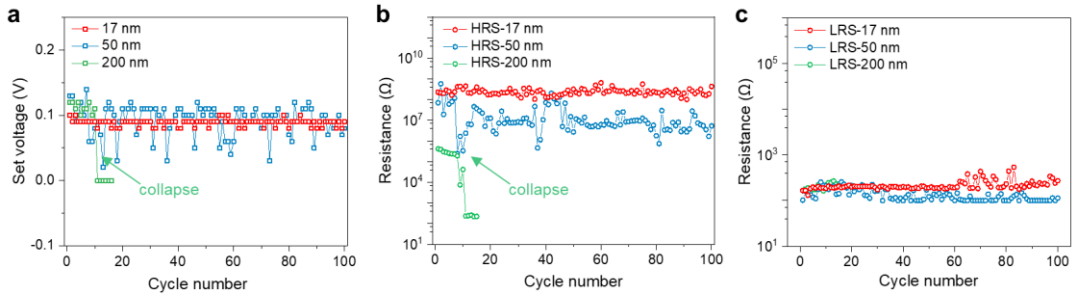

Figure S16. a) Set voltage variation of textile-type memristor units with nanochannel size of 17, 50 and 200 nm. b, c) High resistance state (HRS, b) and Low resistance state (LRS, c) variations of textile-type memristor units with nanochannels size of 17, 50 and 200 nm.

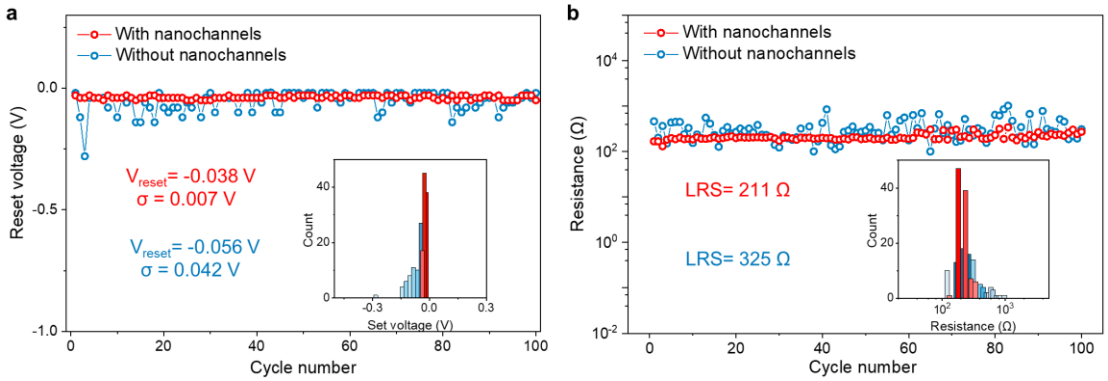

Figure S17. a) Reset voltage variation of textile-type memristor units with and without nanochannels. b) LRS variation of textile-type memristor units with and without nanochannels.

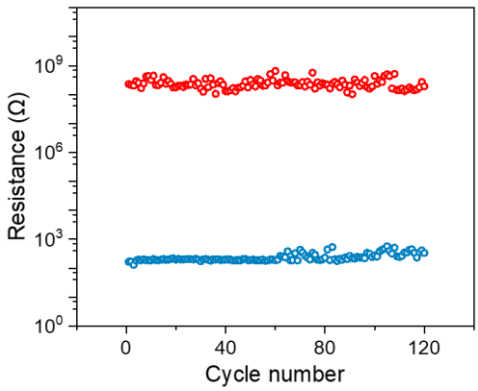

Figure S18. Endurance characteristic of textile-type memristor unit with nanochannels.

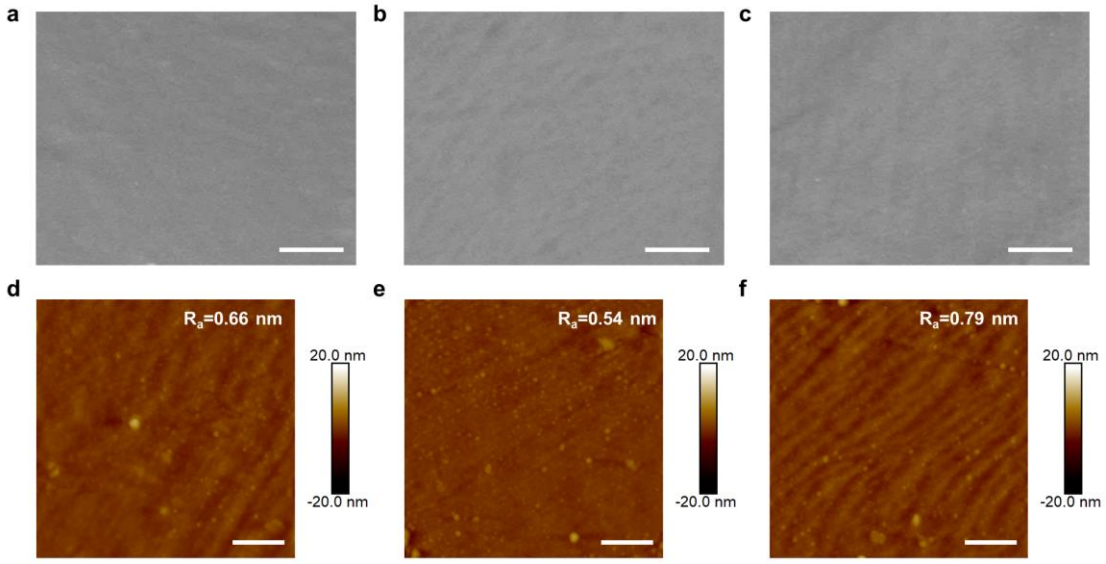

Figure S19. a-c) SEM images of original Ag fiber electrode, after cyclic switching and after sliding operations, respectively. d-f) AFM images of original Ag fiber electrode, after cyclic switching and sliding operations, respectively. Scale bars, 200 nm.

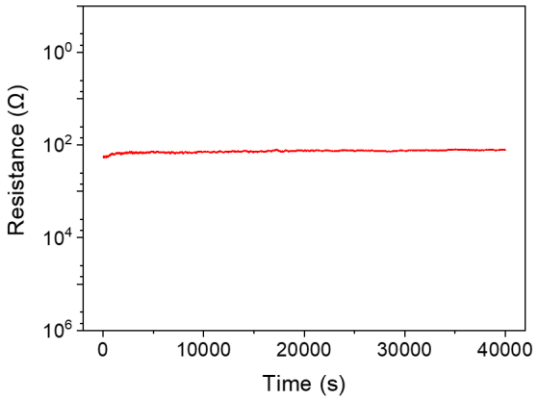

Figure S20. The LRS retention curve of the memristor with nanochannels at 85 ℃.

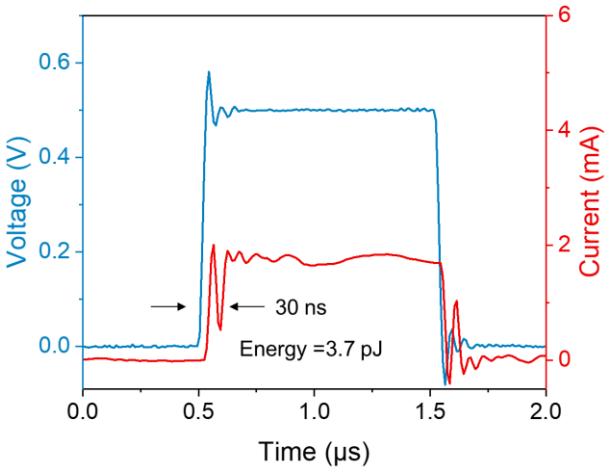

Figure S21. Switching characteristic curves of the memristor through pulse test.

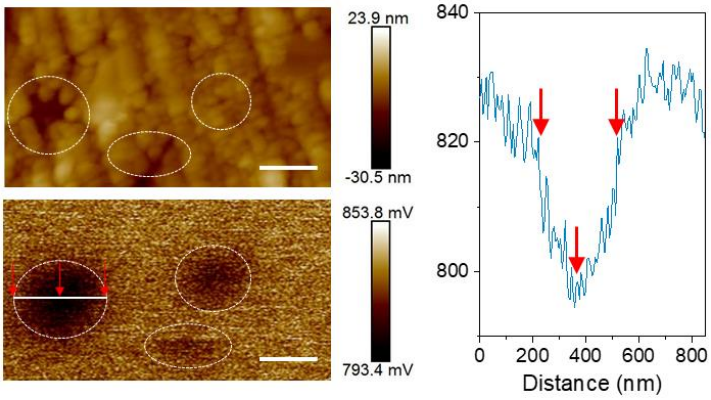

Figure S22. Kelvin probe force microscopy image of nanochannels across the CuZnS film showing that low surface potential was distributed at the nanochannels. Scale bar, 200 nm.

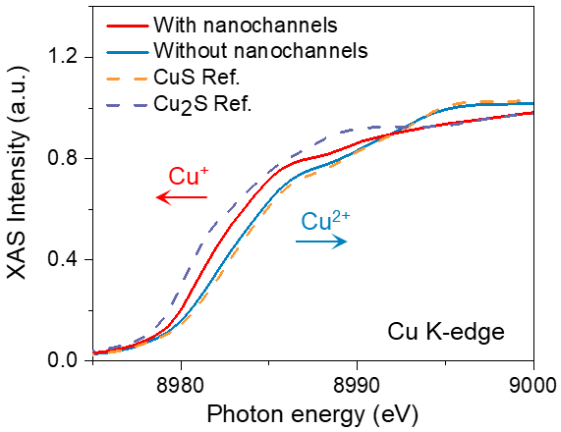

Figure S23. Normalized Cu K-edge X-ray absorption near edge structure spectra of CuZnS film with and without nanochannels.

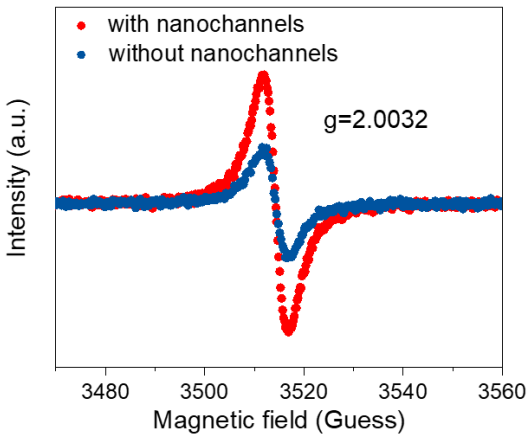

Figure S24. Electron paramagnetic resonance spectra of CuZnS films with and without nanochannels.

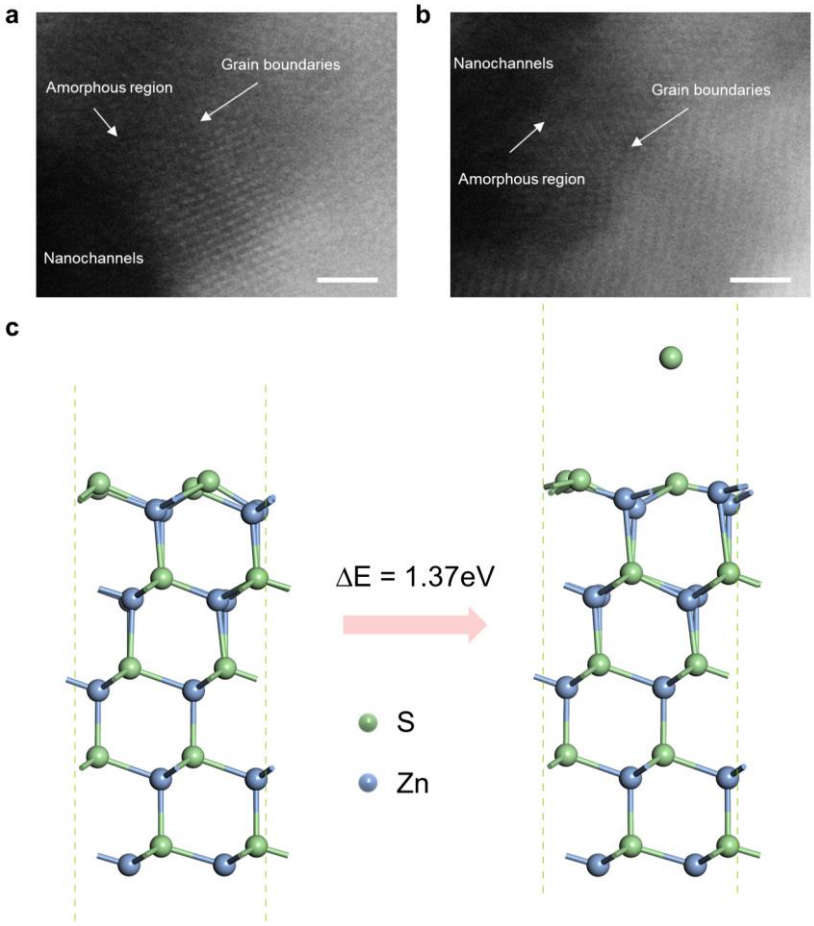

Figure S25. a, b) Atomic-resolution scanning transmission electron microscopy image of S defects in CuZnS film. b) Schematic diagram for the formation of S defects. Scale bar, 5 A (a).

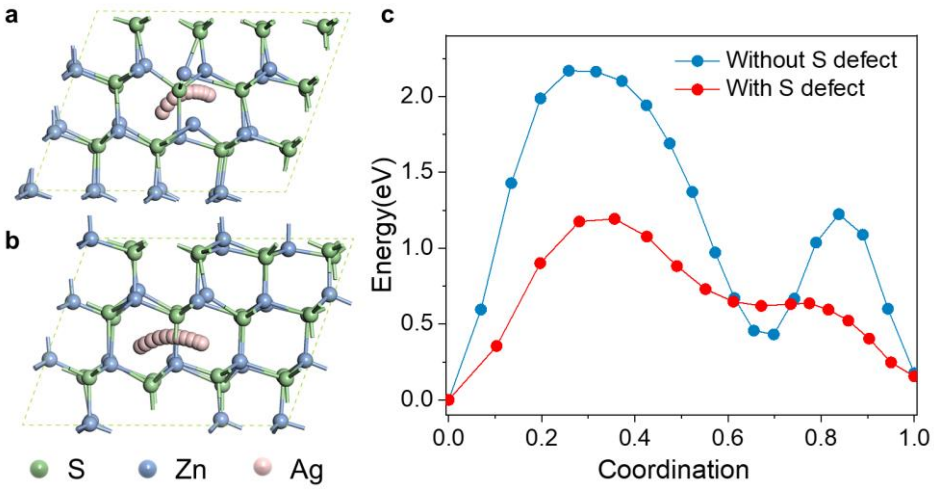

Figure S26. a, b) Schematic diagram of Ag ion migration in the crystal with (a) and

without (b) S defects to simulate the bulk migration process. c) Diffusion energy barriers of Ag ion migration with and without S defects.

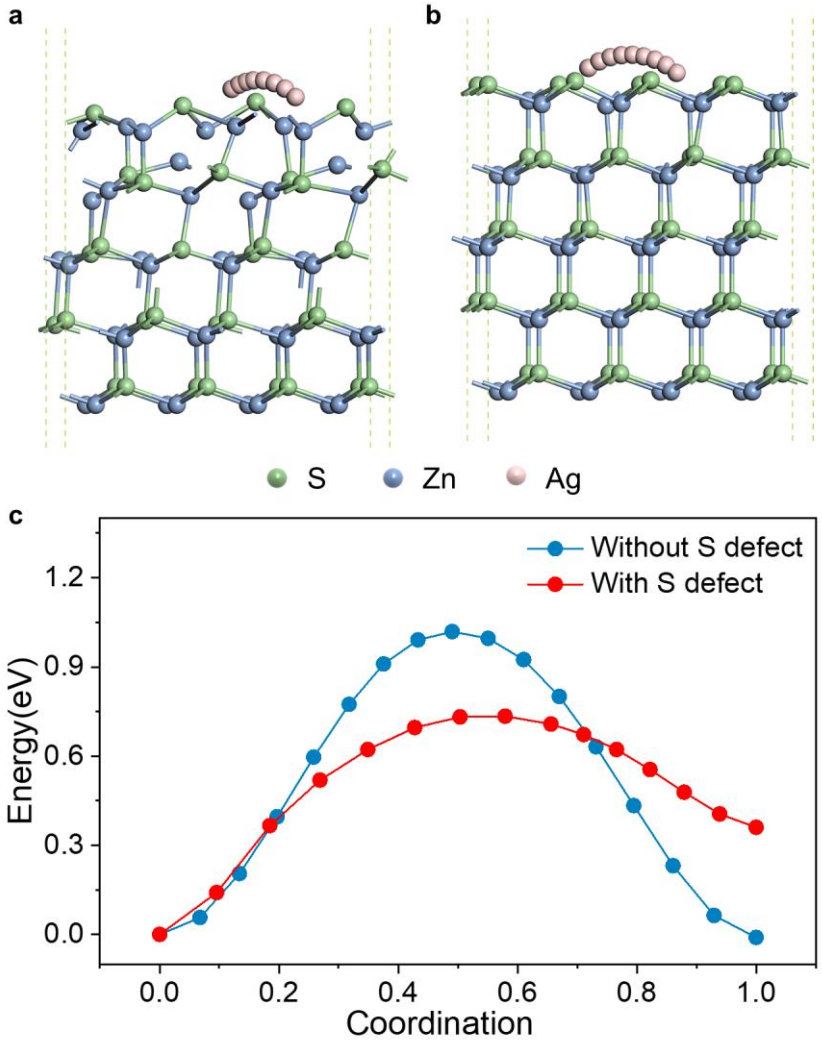

Figure S27. a, b) Schematic diagram of Ag ion migration on the crystal face with (a) and without (b) S defects to simulate the surface migration around the nanochannels. c) Diffusion energy barriers of Ag ion migration with and without S defects.

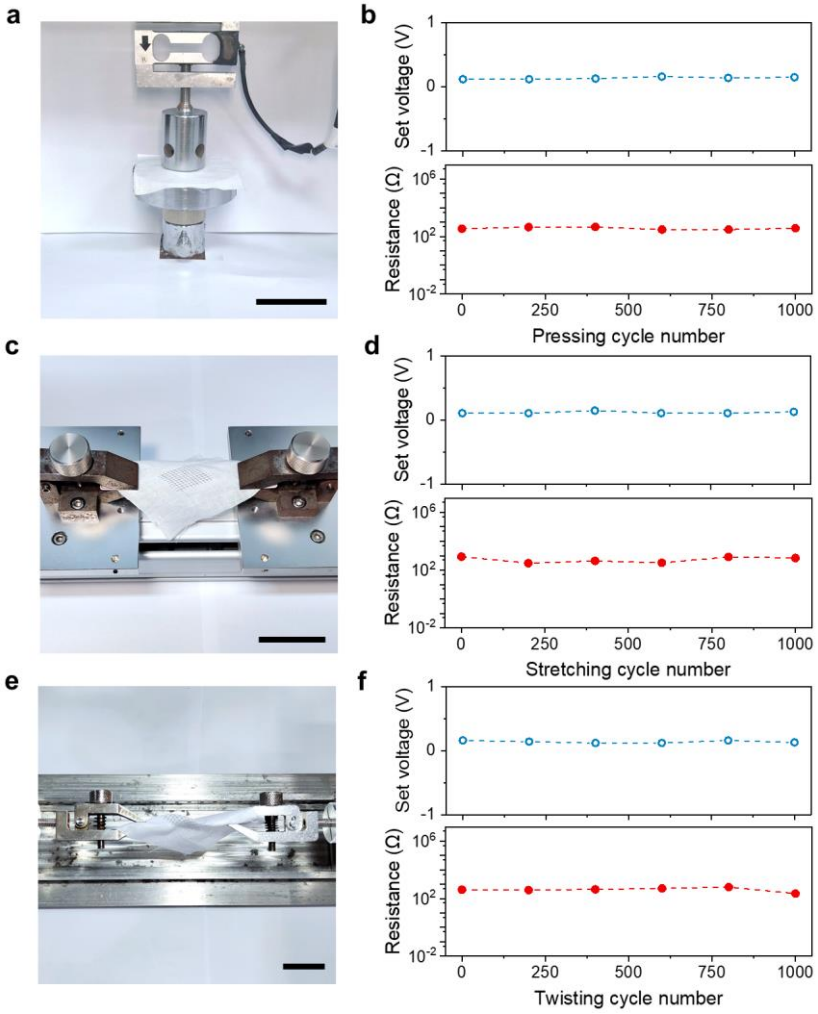

Figure S28. Variations of set voltage and resistance state for textile-type memristor after repeatedly pressed with a pressure of 250 N m^{-2} (a, b), stretched with a strain of 10% (c, d) and twisted with a pitch of 5 cm and curvature radius of 1 cm (e, f). Scale bars, 5 cm (a), 5 cm (c), 2 cm (e).

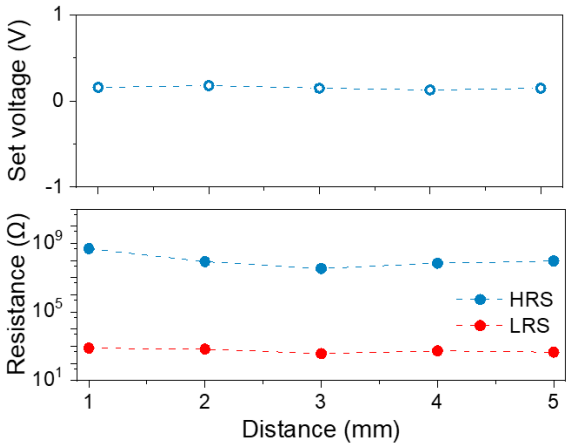

Figure S29. Variations of set voltage and resistance state of textile-type memristor when Pt/CuZnS fiber interlaced at different positions of Ag fiber electrodes.

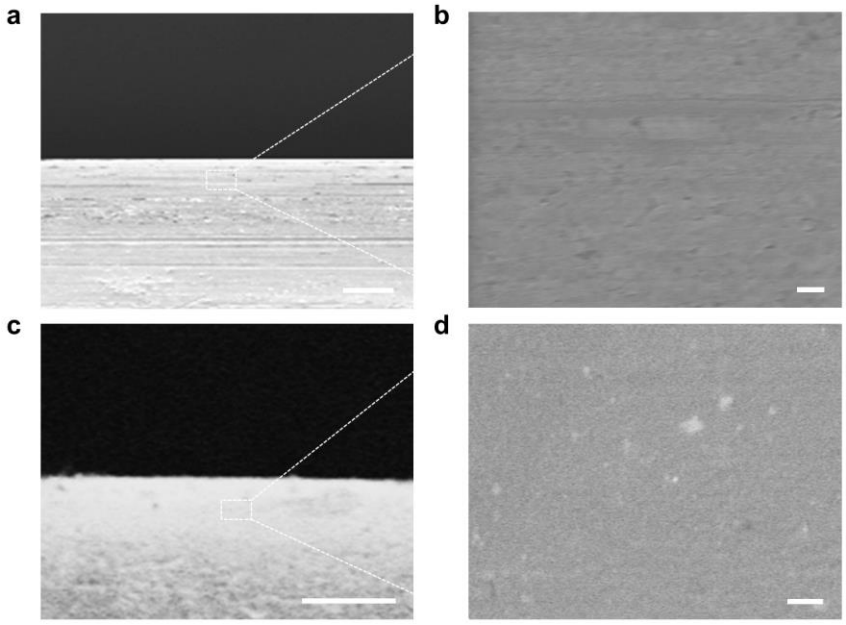

Figure S30. SEM images of Pt (a, b) and Ag (c, d) fiber electrode. Scale bars, 5 μm (a), 200 nm (b), 3 μm (c), 200 nm (d).

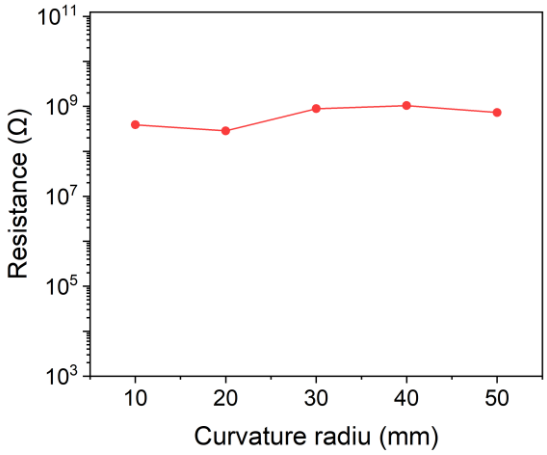

Figure S31. Interface electrical conductance between Pt and CuZnS film when the Pt/CuZnS fiber was bent with different curvature radii.

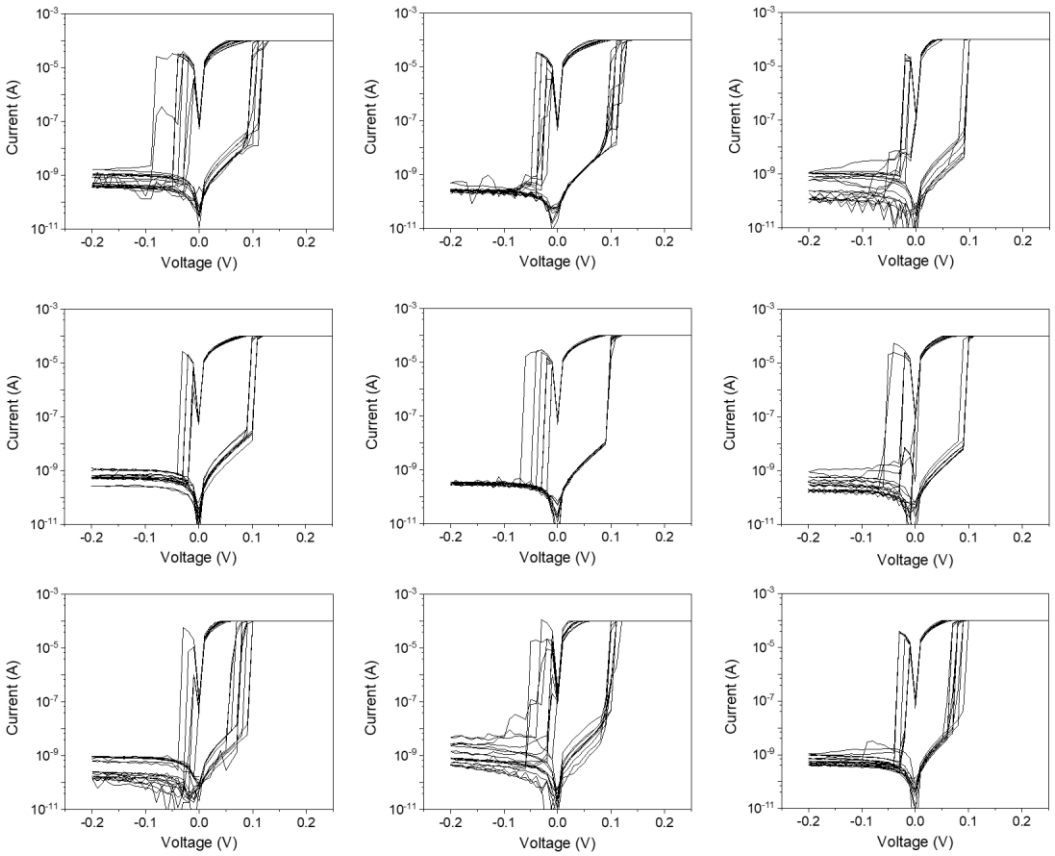

Figure S32. *I-V* curves of nine textile-type memristor units from the 5×5 textile-type memristor array.

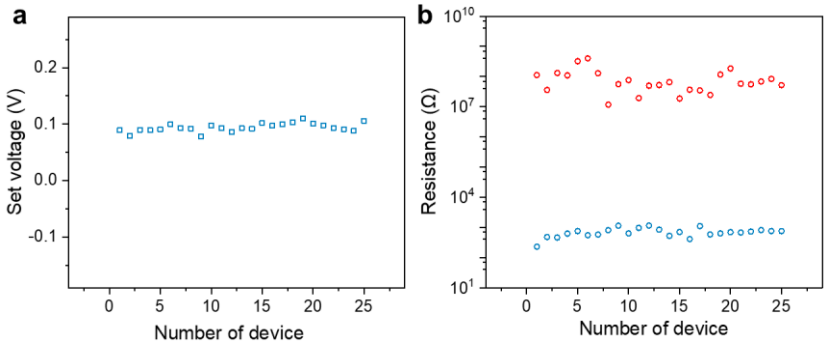

Figure S33. Variations of set voltage (a) and resistance state (b) for memristor units in a 5×5 textile-type memristor array.

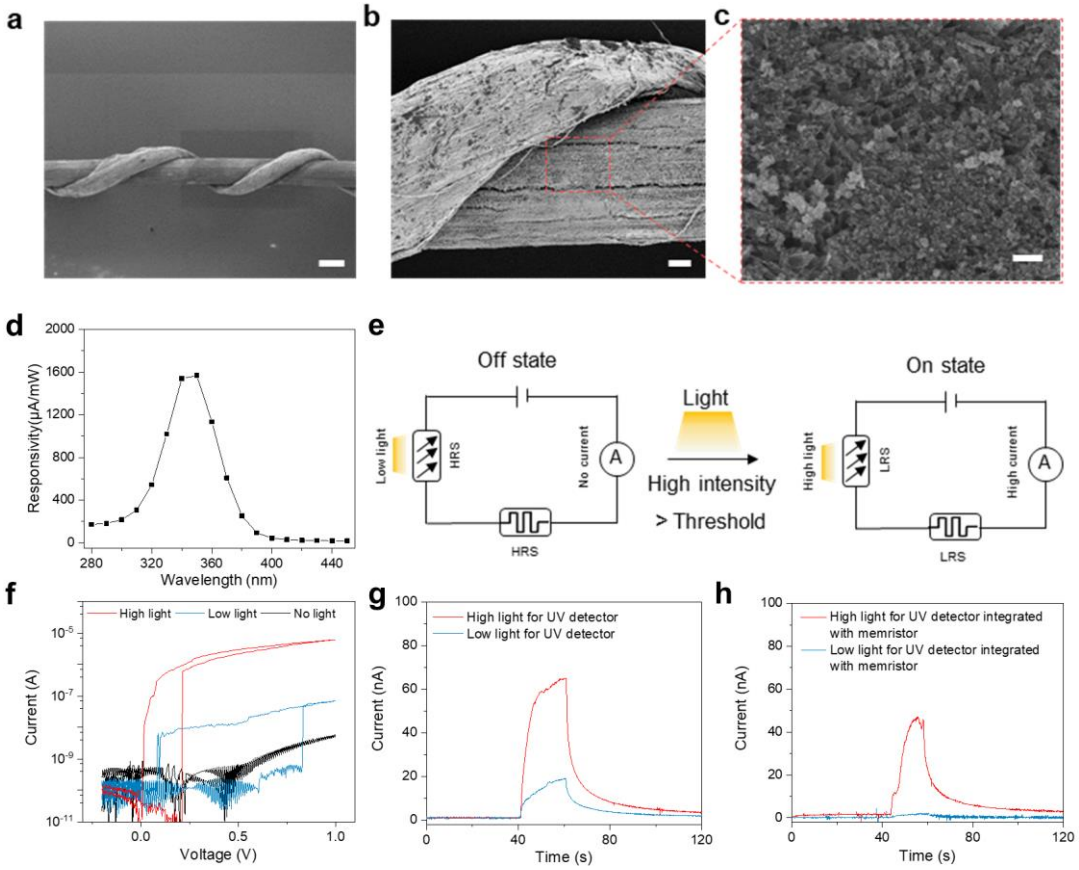

Figure S34. a-c) SEM images of ultraviolet light fiber sensor by twisting Ti wire and carbon nanotube fiber. d) Responsivity of the ultraviolet light fiber sensor as a function of wavelength. **e**, Schematic showing the working mechanism of ultraviolet light sensor integrated with memristor. With the light intensity detected by the ultraviolet light sensor exceeding the threshold value, the memristor will switch to on state and pass a high current flow. f) *I-V* curves of the ultraviolet light sensor integrated with memristor measured under ultraviolet light radiation with low and high intensities. g, h) Photo response of the only ultraviolet light sensor (g) and ultraviolet light sensor integrated with memristor (h) under UV-light radiation with different intensity at 0.6 V bias voltage. Scale bars, 100 μm (a), 20 μm (b), 400 nm (c).

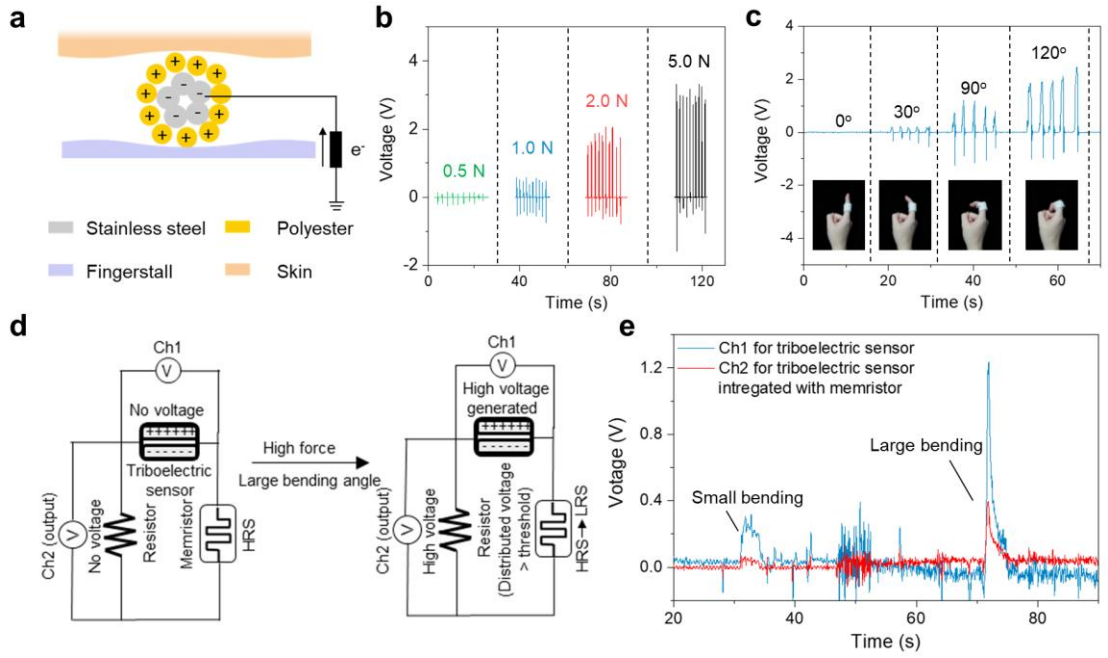

Figure S35. a) Electrical potential distribution of the fiber triboelectric sensor under stretching. b) Voltage signals of the fiber triboelectric sensor when different forces were applied. c) Voltage signals of fiber triboelectric sensor under different bending states of index finger. d) Schematic showing the working mechanism of fiber triboelectric sensor integrated with the memristor. e) Voltage signals of the only triboelectric sensor and triboelectric sensor integrated with memristor under different bending states.

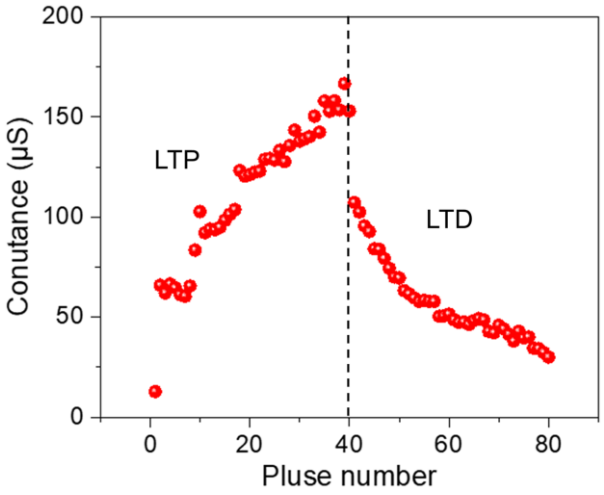

Figure S36. Long-term potentiation (LTP) and long-term depression (LTD) characteristics under 40 consecutive potentiation pulses (0.1 V) and depression pulses (–0.05 V) with pulse width of 50 ms.

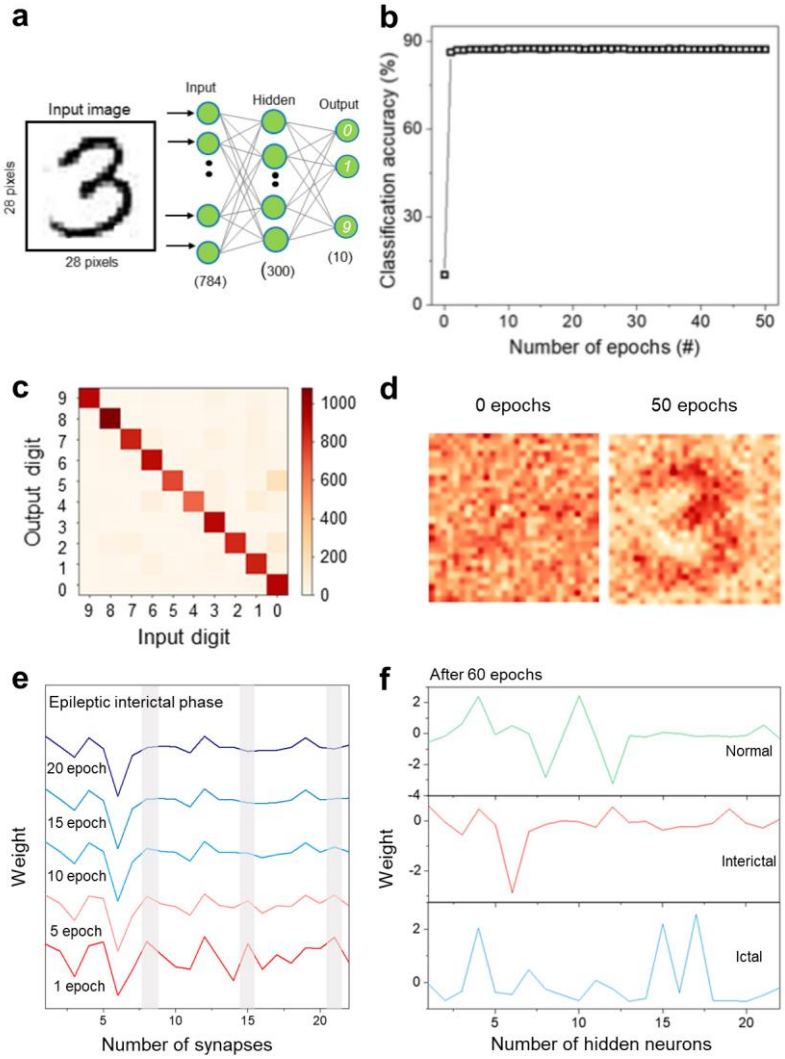

Figure S37. a) Schematic illustration showing a three-layer neural network to recognize representative MNIST handwritten digit "3" (28×28 pixels image). The topology of neural network consists of three layers with 784 input, 300 hidden and 10 output neurons. b) Recognition accuracy for MNIST patterns. c) The confusion matrix for input digit and output digit. d) The reshaped contour images of the digit "3" from synaptic weight before and after 50 epochs. e) Changes in the weight values of artificial synapses correlated to epileptic interictal phase during 20 training epochs. f) The weight values of artificial synapses from Normal, Epileptic interictal phase and Epileptic ictal phase after 60 training epochs.

Table S1. Comparison of the memristive performances of textile-type memristors in this work with the state-of-the-art memristors.

Device structure	materials	Set voltage (V)	Set voltage standard deviation (V)	Set voltage variation (%)	Set power (W)	On/off ratio	Reference
Ag/nanochannel-confined CuZnS/Pt	Chalcogenide	0.089	0.005	5.6%	10^{-10}	10^{6}	This work
Ti/$PdSe_2$/Au	Chalcogenide	0.6	0.047	7.8%	10^{-5}	10^{3}	*Nat. Electron.* 2021, 4, 348-356.
Au/Cr/CuSe/Cr/Au	Chalcogenide	0.4	0.07	17.5%	10^{-5}	10^{2}	*Adv. Mater.* 2022, 34, 2108313.
Cu-Ag alloy/a-Si/Si	amorphous Si	1.8	0.061	3.3%	10^{-6}	10^{4}	*Nat. Nanotechnol.* 2020, 15, 574-579.
Ag/Ga_2O_3/PbS/Pt	Quantum dots	0.19	0.02	10.1%	10^{-9}	10^{6}	*Adv. Mater.* 2019, 31, 1805284.
Ag/$CsPbBr_3$/Pt	Perovskite	0.16	0.013	8%	/	10^{5}	*Adv. Funct. Mater.* 2022, 32, 2201510.
Ag/PMMA/$CH_3NH_3PbI_3$/Au tip/ITO	Perovskite	-0.11	0.03	27%	/	10^{8}	*J. Mater. Chem. C* 2021, 9, 15435-15444.
ITO/ZnO/TaN	Metal oxide	0.48	0.048	10%	/	10^{2}	*Nanoscale* 2020, 12,

							9116-9123.
Ag/SiO_2-Ta_2O_5/Pt	Metal oxide	0.3	0.1	33.3%	10^{-6}	10^3	*Nanoscale* 2020, 12, 4320-4327.
Ag/SiO_2/Pt	Metal oxide	1.113	0.574	51.6%	10^{-6}	10^2	*ACS Nano* 2016, 10, 9478-9488.
Ag/SiO_2/Pt	Metal oxide	0.273	0.088	32.2%	10^{-6}	10^2	*ACS Nano* 2016, 10, 9478-9488.
Pt/HfO_2-AgD30/Ti	Doping metal NPs (Ag NPs)	0.4	0.12	30 %	/	10^3	*Adv. Funct. Mater.* 2019, 29, 1808430.
Pt/HfO_2-TiD30/Ti	Doping metal NPs (Ti NPs)	0.94	0.14	14.9%	/	10^2	*Adv. Funct. Mater.* 2019, 29, 1808430.
ITO/$Ru(L)_3](PF6)_2$-Au NPs/ITO	Doping metal NPs (Au NPs)	0.519	0.03	5.7%	10^{-10}	10^3-10^5	*Nat. Mater.* 2017, 16, 1216-1224.
Ag/2DPBTA+PDA/ graphene	Organic material	0.9	0.15	16.7%	10^{-8}	10^2-10^5	*Adv. Mater.* 2019, 31, 1902264.
Al/PVK/ITO	Organic material	1.4	0.8	57.1%	10^{-4}	10^3	*Adv. Mater.* 2017, 29, 1701333.

Ag/N-$CuMe_2Pc$/ITO	Organic material	0.5	0.2	40%	10^{-6}	10^4	*Adv. Electron. Mater.* 2019, 5, 1800793.
Au/SrCoOx/$SrRuO_3$	Brownmillerite oxides	3.98	0.072	1.8%	/	10^4	*Sci. Adv.* 2021, 7, eabh0648.
Ag/i-SiGe(NP)/p-Si	Alloy semiconductor	4	0.04	1%	/	10	*Nat. Mater.* 2018, 17, 335-340.

Table S2. Atomic percentage of Ag element from XPS spectra at the interfacial region between nanochannel-contained CuZnS film and Ag electrode. The applied set voltages were 0, 0.02 and 0.1 V.

Voltage (V)	**Ag at%**
0.1	0.23
0.02	0.02
0	0.01

Table S3. Textile properties of the memristors through standard tests.

Test item	**Textile property index**	**Test standard**	**Test result**
Breathability test	Air permeability	GB/T 5453-1997	1747 mm/s
Moisture permeability test	Water-vapour transmission	GB/T 12704.2-2009	3.96×10^3 g/(m^2·24h)
Drape test	Drape coefficient	GB/T 23329-2009	58.3%

Supplementary Reference

[1] X. Xu, J. Bullock, L. T. Schelhas, E. Z. Stutz, J. J. Fonseca, M. Hettick, V. L.

Pool, K. F. Tai, M. F. Toney, X. Fang, A. Javey, L. H. Wong and J. W. Ager, *Nano. Lett.* **2016**, 16, 1925.

[2] S. W. Shin, G. L. Agawane, M. G. Gang, A. V. Moholkar, J. H. Moon, J. H. Kim and J. Y. Lee, *J. Alloys Compd.* **2012**, 526, 25.

[3] X. Xu, J. Chen, S. Cai, Z. Long, Y. Zhang, L. Su, S. He, C. Tang, P. Liu, H. Peng and X. Fang, *Adv. Mater.* **2018**, 30, 1803165.

[4] Z. Zhou, K. Chen, X. Li, S. Zhang, Y. Wu, Y. Zhou, K. Meng, C. Sun, Q. He, W. Fan, E. Fan, Z. Lin, X. Tan, W. Deng, J. Yang and J. Chen, *Nat. Electron.* **2020**, 3, 571.

[5] K. Meng, S. Zhao, Y. Zhou, Y. Wu, S. Zhang, Q. He, X. Wang, Z. Zhou, W. Fan, X. Tan, J. Yang and J. Chen, *Matter* **2020**, 2, 896.

[6] J. He, C. Lu, H. Jiang, F. Han, X. Shi, J. Wu, L. Wang, T. Chen, J. Wang, Y. Zhang, H. Yang, G. Zhang, X. Sun, B. Wang, P. Chen, Y. Wang, Y. Xia and H. Peng, *Nature* **2021**, 597, 57.

[7] C. S. Yang, D. S. Shang, N. Liu, E. J. Fuller, S. Agrawal, A. A. Talin, Y. Q. Li, B. G. Shen and Y. Sun, *Adv. Funct. Mater.* **2018**, 28, 1804170.

[8] E. J. Fuller, F. E. Gabaly, F. Léonard, S. Agarwal, S. J. Plimpton, R. B. Jacobs Gedrim, C. D. James, M. J. Marinella and A. A. Talin, *Adv. Mater.* **2017**, 29, 1604310.

[9] Y. Dai, C. Ma, X. Zhang, F. Wang, W. Lu, J. Yang and F. Yang, *AIP Adv.* **2017**, 7, 085308.

[10] J. P. Perdew, K. Burke and M. Ernzerhof, *Phys. Rev. Lett.* **1996**, 77, 3865.

[11] N. Govind, M. Petersen, G. Fitzgerald, D. King Smith and J. Andzelm, *Comput. Mater. Sci.* **2003**, 28, 250.